www.elsevier.com/locate/ijadhadh

The Measurement of Damage Initiation, Particle Adhesion and Cohesive Strength from Traction Displacement Curves of a Nano-toughened Epoxy

D. Mc Auliffe, A. Karac, N. Murphy, A. Ivankovic

PII: S0143-7496(16)30089-6
DOI: http://dx.doi.org/10.1016/j.ijadhadh.2016.04.014
Reference: JAAD1842

To appear in: *International Journal of Adhesion and Adhesives*

Received date: 14 August 2015
Accepted date: 26 April 2016

Cite this article as: D. Mc Auliffe, A. Karac, N. Murphy and A. Ivankovic, The Measurement of Damage Initiation, Particle Adhesion and Cohesive Strengtl from Traction Displacement Curves of a Nano-toughened Epoxy, *Internationa Journal of Adhesion and Adhesives* http://dx.doi.org/10.1016/j.ijadhadh.2016.04.014

The Measurement of Damage Initiation, Particle Adhesion and Cohesive Strength from Traction Displacement Curves of a Nano-toughened Epoxy

D. Mc Auliffe[a], A. Karac[b], N. Murphy[a], A. Ivankovic[a,*]

[a]*School of Mechanical and Materials Engineering, University College Dublin, Belfield, Dublin 4, Ireland*
[b]*Masinski fakultet u Zenici, Fakultetska 1, 72000 Zenica, Bosna i Hercegovina*

Abstract

In this work the deformation behaviour of a nano toughened epoxy adhesive is measured at different levels of stress triaxiality. The test method consists of a notched axisymmetric adhesive layer loaded in tension. The recorded traction displacement curves were analysed numerically and it was found that the measured peak stress corresponds to the intrinsic cohesive strength, σ_{max} of the material. This method allows experimental measurement of σ_{max} for use in cohesive zone models of fracture. Additional features of the traction displacement curves include a kink that corresponds to particle debonding at a critical hydrostatic stress. By application of the Mori-Tanaka model, the relationship between the experimental measurements and particle/matrix adhesion is described.

Keywords: Nano-particles, adhesive joints, toughening mechanisms, cohesive strength

1. Introduction

Epoxy based structural adhesives have been toughened by second phase particles for many years. More recently, nano-sized particles have been added to epoxies to produce adhesives with fracture energies over an order of magnitude greater than their epoxy matrix alone. For nano-toughened adhesives, this increase in fracture energy is derived from localised plasticity that occurs due to the presence of the particles. The two primary mechanisms are growth of voids initiated by particle debonding or cavitation, and plastic shear bands which develop between particles/voids [1, 2, 3, 4, 5].

Adhesive joint fracture is often modelled using a cohesive zone model (CZM) [6, 7, 8]. The CZM is governed by a traction separation law (TSL), which relates the separation of opposing fracture surfaces to the traction across them. This approach is preferred to modelling the mechanisms of material separation directly since the length scales involved differ by several orders of magnitude. The critical parameters of a traction separation law are the intrinsic fracture energy G_0 and the maximum cohesive strength σ_{max}. If the CZM is coupled with an elastic plastic continuum the total fracture energy G_C is the sum of energy dissipated in the CZM, G_0, and the plastic energy dissipated in the continuum, G_p, i.e.

$$G_C = G_0 + G_P \tag{1}$$

Tvergaard and Hutchinson[9] noted that the ratio of the σ_{max} to the yield stress σ_y must be greater than 2.5 for G_P to be significant compared to the G_0. The cohesive strength is often assumed to be greater than the strength of the material under uniaxial tension due to the constraint effects during fracture. Pardoen et al. [6] used a CZM described by a single TSL (i.e. constant G_0 and σ_{max}) with $\sigma_{max}/\sigma_y > 3$ coupled to an elastoplastic adhesive layer to model the fracture of adhesive joints of different thickness and obtained close agreement. Cooper et al. [10] modelled the fracture behaviour of Tapered Double Cantilever Beam

*Corresponding author
Email address: Alojz.ivankovic@ucd.ie (A. Ivankovic)

(TDCB) tests conducted over a range of bond gap thicknesses using a variable TSL, with $\sigma_{max}/\sigma_y < 2$ in all cases and found that G_0 accounted for most of the energy dissipation.

Another approach [11] employs critical distance theory whereby fracture occurs when a failure stress at a critical distance is reached. The critical distance and failure stress were determined by inverse analysis, and it was demonstrated that the critical distance related to microstructural features. With this model $\sigma_{max}/\sigma_y > 3$ was used.

Clearly the details of energy dissipation and interpretaion of numerical analyses is highly dependent on the set of cohesive parameters chosen to simulate fracture. Studies regularly rely on inverse analysis to determine the value for σ_{max} and G_0 [12, 6] whereby the parameters are varied until satisfactory agreement is obtained. Indeed it has been shown that multiple combinations of σ_{max} and G_0 produced agreement with experimental results [13, 10]. Therefore, direct experimental measurement of σ_{max} is desirable to define a TSL.

The fracture behaviour of most materials is sensitive to the degree of stress triaxiality at the crack tip. High stress triaxiality suppresses yielding which encourages alternative fracture processes to occur. The mechanisms of fracture for nano-toughened adhesives are primarily shear banding and plastic void growth and their development is affected by the stress triaxiality [14, 2, 15]. Therefore it is useful to characterise material behaviour under conditions of high stress triaxiality. A common measure of stress triaxiality, H, is given as:

$$H = \frac{\sigma_{hyd}}{\sigma_{vm}} \tag{2}$$

where, σ_{hyd} is the hydrostatic stress and σ_{vm} is the von Mises stress.

Some studies have investigated the effects of stress triaxiality on the deformation behaviour of bulk materials using a tensile specimen containing an axisymmetric notch. Deformation is localised to the notched region due to the reduced cross-sectional area, but the stress state also becomes triaxial across the remaining ligament. The degree of stress triaxiality is dependent on the depth and geometry of the notch as well as the elastic constants of the material [10, 16, 17, 18]. Pardoen et al. [19] studied void growth in copper bars using this technique. H was increased from 0.4 to 1.6 by using round notches with smaller radii. Katnam et al. [20] followed a similar approach with a toughened adhesive. With smaller notch radii the triaxiality increased but its distribution also became less uniform due to the greater stress concentration around the notch. The experimental work revealed that under conditions of increasing constraint the strength of the adhesive also increased. Cooper et al. [10] observed similar behaviour on a nano and micro-toughened adhesive using a circumferentially deep notched tensile (CDNT) specimen, with constraint varied by notch depth. Numerical simulations of the tests revealed that H varied between 1 and 1.4, below the level experienced ahead of the crack tip in Tapered Double Cantilever Beam fracture tests.

Another triaxial test method, known as the butt-joint or poker chip test consists of two stiff substrates bonded over a given adhesive layer thickness. The stiff substrate restricts the Poisson's contraction of the adhesive layer thereby increasing the stress triaxiality [21]. The failure strain under these conditions is reduced compared with uniaxial tensile tests [21]. Elevated stress triaxialities with the method are limited by premature interfacial failure due to the singularity that exists at the material interface.

In this work it is attempted to experimentally measure the cohesive strength of a nano-toughened adhesive at different levels of stress triaxiality.The procedure combines features of the methods above to achieve values of H that are comparable to adhesive joint fracture, without the stress concentrations seen in other methods. This will enable direct measurement of σ_{max} for accurate modelling of the adhesive layer. Additionally, the measured traction separation curve is examined in detail which allows the conditions for damage initiation and particle decohesion to be identified.

2. Experimental Materials and Procedures

2.1. Materials

Two materials have been studied in this work. The first is a single part hot cured epoxy based on Epon 828 cured with Dicyandiamide. Further components have been added to this formulation to improve its

performance but this remains proprietary information. For the remainder of this work, this material shall be referred to as the matrix. The second material is a toughened adhesive, consisting of the same matrix with two grades of core-shell-rubber (CSR) nanoparticles added simultaneously. The first particle is Kaneka MX153 (Kaneka Corporation, USA) with a measured average diameter of 66 nm and the second is Zeon F351 (Zeon Corporation, Japan) with average particle diameters of 200 nm, these particles occupy 16 Vol% and 22 Vol% respectively. TDCB testing on the identical system has shown a 12 fold increase in the fracture energy of the toughened adhesive compared to the neat matrix [22, 7, 10, 23]. A CSR particle consists of a rubber core surrounded by a glassy polymeric shell. The cure schedule for both materials is 180°C for 90 minutes.

2.2. Thermal Analysis

Differential scanning calorimetry was used to measure the glass transition temperature T_g of the matrix and toughened adhesive. Samples were heated at a rate of 10°/min, and the glass transition was identified by a rapid change in specific heat capacity using the midpoint method [24]. It was found that for the matrix $T_g = 375.85$ K and for the toughened adhesive $T_g = 380.25$ K. Since the values are in relatively close agreement it can be assumed that the mechanical properties of the matrix in the toughened adhesive are equivalent to the bulk matrix [5].

2.3. Bulk Deformation Behaviour

Uniaxial tension, uniaxial compression and plane strain compression tests were completed on both the matrix and toughened adhesive samples. All tests were conducted at low loading rates and ambient temperature. For each test configuration a minimum of three repeats were performed.

2.3.1. Manufacture of Bulk Samples

The preparation of bulk samples for each mechanical test method closely followed the guidelines provided by standard BS ISO 15166-2:2000 [25]. Plates of material were cured in aluminium moulds, and then machined to their final geometry. In the case of tensile test specimens the machined surfaces were polished manually using 1200 grit emery paper to remove any defects produced by the machining process.

2.3.2. Uniaxial Tension Tests

Uniaxial tensile tests were conducted according to ISO 527 with a sample geometry according to the B configuration. The samples were tested in a screw driven tensile testing machine at a crosshead displacement rate of 0.1 mm/min. The load, P, was measured by a 5 kN load cell and the elongation of the gauge length Δl_A and reduction in width Δl_T of the specimen were determined using non-contact video extensometry. This allowed the calculation of axial strain $\epsilon_A = \frac{\Delta l_A}{l_A}$, the transverse strain $\epsilon_T = \frac{\Delta l_T}{l_T}$, the Poisson's ratio $\nu = \frac{-\epsilon_T}{\epsilon_A}$, Young's Modulus E and yield stress σ_y from each test.

2.3.3. Uniaxial Compression Tests

The uniaxial compression test setup consisted of two polished platens connected to a mechanical testing machine. A PTFE sheet was placed on each platen and molybdenum disulfide grease was used to lubricate the surfaces. The sample was placed at the centre of the bottom platen and loaded to 50 kN. Samples were produced with a radius and height of 5mm. The sidewalls of the sample were monitored during compression and it was found that neither buckling nor barrelling occurred. From each test a stress-strain curve was recorded and E and σ_y were calculated.

2.3.4. Plane Strain Compression Tests

The plane strain compression (PSC) test is primarily used in this work to evaluate the yield behaviour of the materials under a multiaxial stress state. The method, which has been employed many times by Boyce and co-workers [26], involves a stiff die and punch that have ground and polished surfaces. A rectangular block with the same thickness as the channel is made from the material to be tested. The punch, manufactured to have a sliding fit with the die, compresses the block of material in the die. The stiff sidewalls prevent

strain normal to their surface, but the material is free to flow in the other transverse direction. The setup for this work can be seen in Fig. 1. The internal surfaces were lubricated with molybdenum disulfide grease; previously this setup has reduced the effects of friction to a negligible level [27]. The specimen dimensions were 15 x 10 x 6 mm. For the uniaxial tension and uniaxial compression tests the Young's modulus, E, is taken as the slope of the initial linear region of the stress strain curve but for the plane strain compression tests the slope must be corrected to account for the multiaxial stress state. This is calculated as

$$E = (1 - \nu^2)E^{ps} \tag{3}$$

where E^{ps} is the plane strain modulus, i.e. the slope of the linear region of the PSC stress-strain curve.

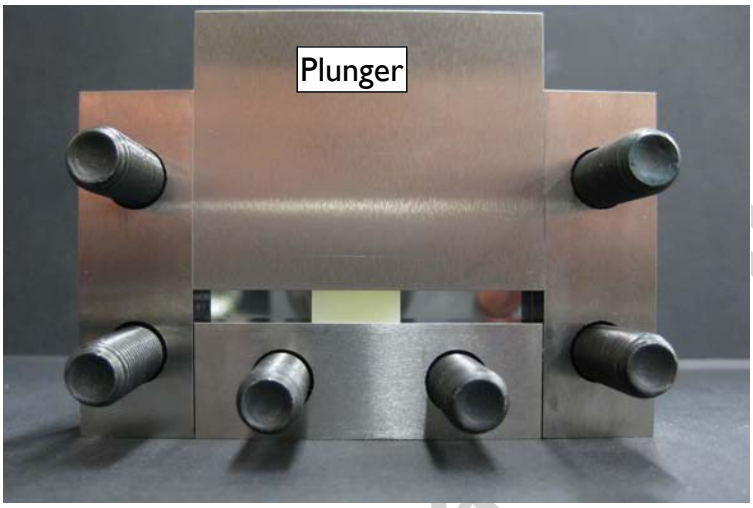

Figure 1: Test rig for plane strain compression tests with one sidewall removed.

2.4. CDNT Tests

2.4.1. Development of the Bonded CDNT Test Method

To overcome the limitations of a bulk CDNT specimen a modified test method is proposed. The configuration consists of two mild steel substrates bonded over a certain bond gap thickness with a notch machined into the adhesive layer. The stress triaxiality is elevated by both the presence of the notch and the substrate but unlike in previous bulk specimens a very sharp notch is unnecessary to produce a high constraint. Therefore a stress distribution with greater uniformity is expected.

A disadvantage of this geometry is that the joint preparation must be sufficient to resist interfacial failure. This became an issue during the work and was partially resolved by surface treatment of the substrate. Another consideration is the alignment of the substrates and loading apparatus. Any eccentricity will result in premature failure as the stress is distributed unevenly around the ligament. A schematic of the specimen geometry, including the relevant dimensions is shown in Fig. 2. Wire gauge markings are attached to the steel substrates for recognition by the video extensometer. Full details of sample preparation are described in [23].

2.4.2. Test Method

A precision loading rig with pivot points was used to ensure that only normal loading was applied to the specimen. Specimens were loaded in tension at a crosshead displacement rate of 0.1 mm/min. Three geometries were produced with bond gap thicknesses of 1.0, 1.6, and 2.5 mm. These bond gaps were chosen to produce levels of stress triaxiality that are similar to conditions in the vicinity of the crack tip during fracture, and are also practicable for manufacture. These specimens are shown in Fig. 3. Four specimens

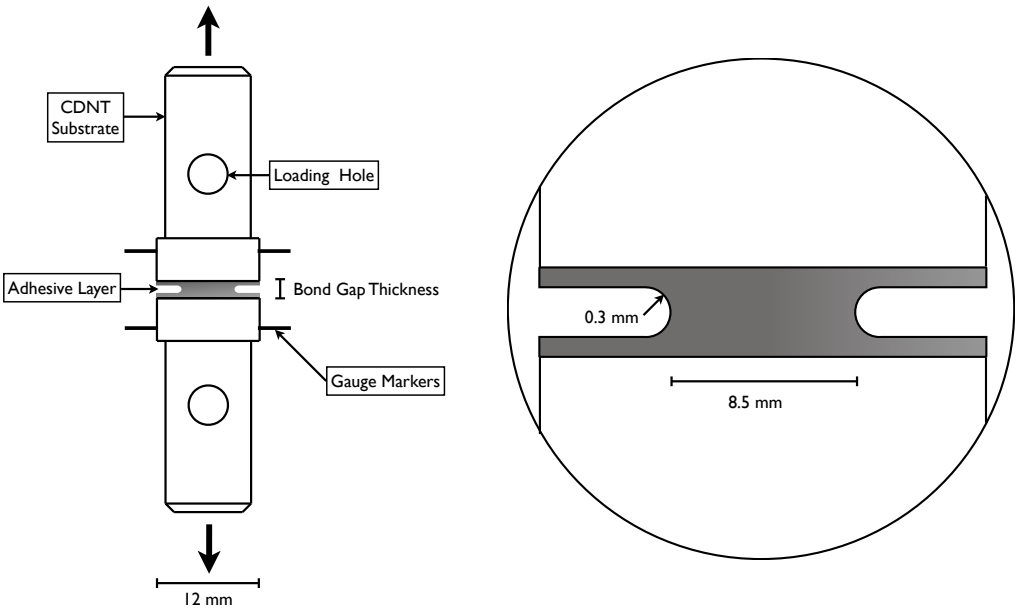

Figure 2: Schematic of the bonded CDNT specimen.

Table 1: Measured mechanical properties of the matrix, note the plane strain compression Modulus is corrected using Eq. 3.

Test	$\sigma_y^{0.2}$ (MPa)	σ_y^{max} (MPa)	E (GPa)	ν
Tension	63.4 ± 0.3%	89.3 ± 0.3%	3.00 ± 2%	0.36 ± 5%
Compression	89.6 ± 1%	127.8 ± 0.3%	3.2 ± 6%	
PSC	139 ± 2%	156 ± 2%	3.1± 4%	

from each bond gap were tested until failure. In addition, a number of samples were unloaded prior to failure at different levels of extension.

The load over the ligament, from which the corresponding ligament traction was computed, and the displacement of the markings were recorded throughout the test.

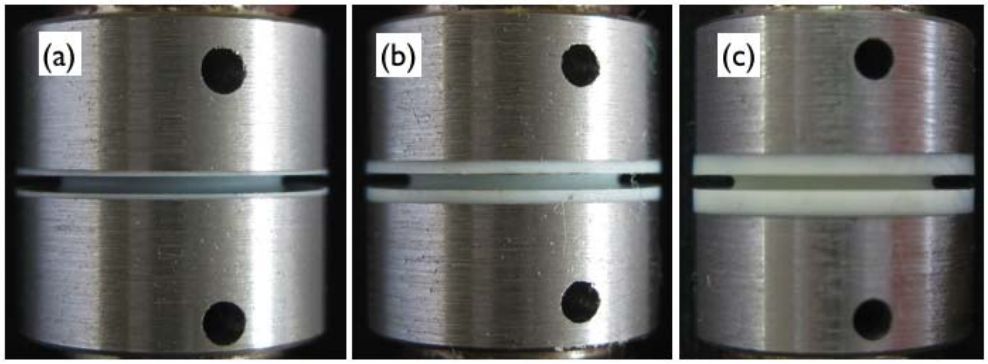

Figure 3: Three CDNT specimens of Bond Gap Thickness (a) 1.0 mm, (b) 1.6 mm and (c) 2.5 mm.

2.5. Fracture Surface Analysis

The fracture surfaces of the CDNT specimens were inspected using scanning electron microscopy. Representative samples from each bond gap thickness were selected and sections were removed. Every section underwent the same gold sputter coating cycle at a current of 30 mA for 30 seconds. In some cases, a conductive strip was attached between the top of the adhesive layer and the mounting stub prior to gold coating to ensure the surface of the specimen was grounded.

3. Experimental Results

3.1. Bulk Deformation results

3.1.1. Matrix Properties

The typical stress strain curves obtained from the bulk deformation tests are shown in Fig. 4 and the corresponding mechanical properties are given in Table 1. The Young's modulus was found to be in close agreement for all test methods but the yield stress varied significantly. This is a common feature of epoxy resins and is attributed to pressure dependent yielding, see [23].

It should be noted that two measures of the yield stress are provided: $\sigma_y^{0.2}$ is the 0.2% offset yield stress, the intersection point between the stress-strain curve and a line with slope equal to the Young's modulus that is offset from the origin by a strain of 0.002 mm/mm, and σ_y^{max}, the first local maximum of the stress-strain curve.

Table 2: Measured mechanical properties of the toughened adhesive for various test methods, note that the plane strain compression modulus is corrected using Eq. 3.

Test	$\sigma_y^{0.2}$ (MPa)	σ_y^{max} (MPa)	E (GPa)	ν
Tension	29.0 ± 0.5%	45.2 ± 1%	1.79 ± 1%	0.42 ± 4%
Compression	36.7 ± 1%	-	1.89 ± 2%	
PSC	49.3 ± 0.9%	-	1.48 ± 3%	

3.1.2. Toughened Adhesive Properties

The measured stress-strain curves and associated properties for the toughened adhesive are given in Fig. 4 and Table 2. It should be noted that σ_y^{max} was not defined for all tests due to the strain hardening behaviour of the adhesive. The Mori-Tanaka [28] model has been employed to predict the elastic properties of the toughened adhesive based on the properties of the matrix and CSR particles. The details of implementation are provided in [23]. This results in a calculated modulus and Poisson's ratio for the toughened adhesive of 1.83 GPa and 0.40 respectively, which are in close agreement with the experimental results.

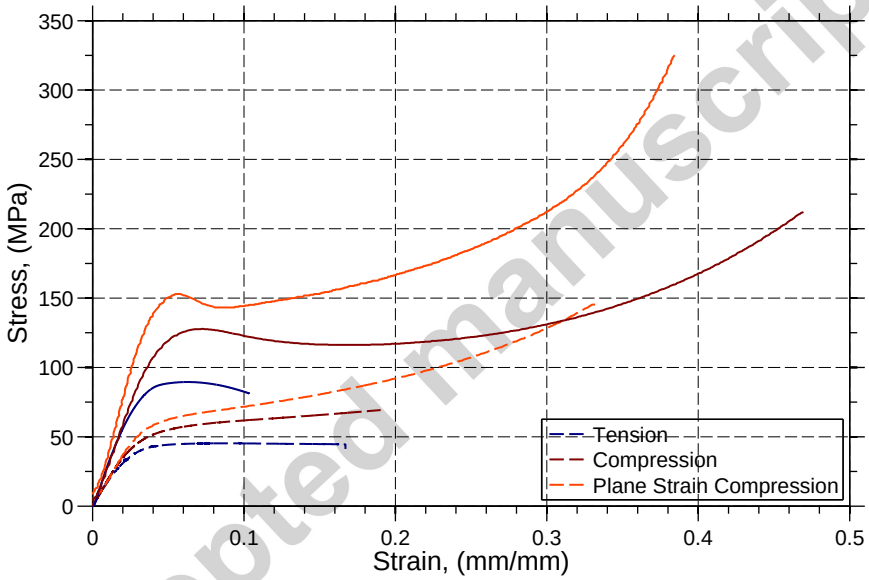

Figure 4: Uniaxial tension, uniaxial compression and plane strain compression test results for the neat adhesive (solid lines) and toughened adhesive (dashed lines).

3.2. CDNT Results

The recorded traction displacement curves of the toughened adhesive, for the CDNT specimens with bond gap thicknesses of 1.0, 1.6 and 2.5 mm are shown in Fig. 5. Clearly there is excellent intersample agreement for all tests except for those with a bond gap thickness of 1.0 mm, where most specimens failed prematurely due to interfacial fracture. For the other bond gap thicknesses cohesive failure was always obtained. For all tests that failed cohesively the peak stress, σ_{peak} was very close to 52 MPa. Also, all specimens demonstrate an abrupt change in slope or "kink" after the initial linear region. This is in contrast with the deformation behaviour under uniaxial tension where there is a gradual transition into non-linear deformation, as shown in Fig. 4.

Representative stress-displacement curves of the tests at each bond gap are displayed in Fig. 6. With a decreasing bond gap thickness, the stiffness of the specimens increases due to: (i) the shorter gauge length and (ii) the corresponding increase in stress triaxiality. It will be shown later that the triaxiality is 2.09,

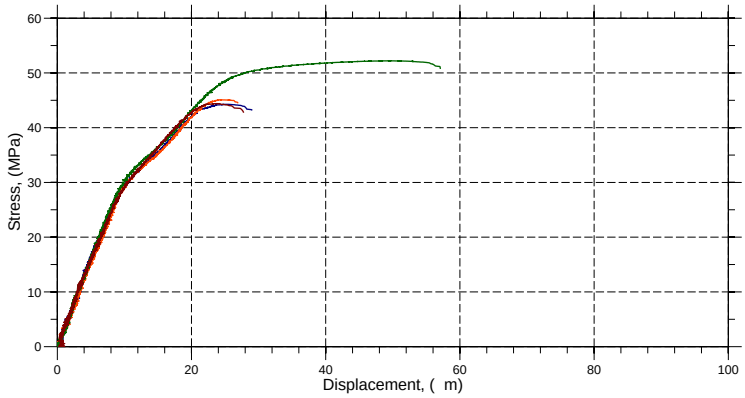

(a) Bond gap thickness = 1.0 mm

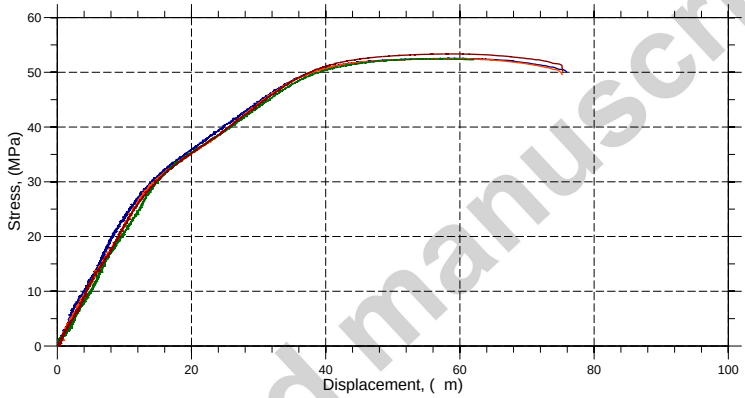

(b) Bond gap thickness = 1.6 mm

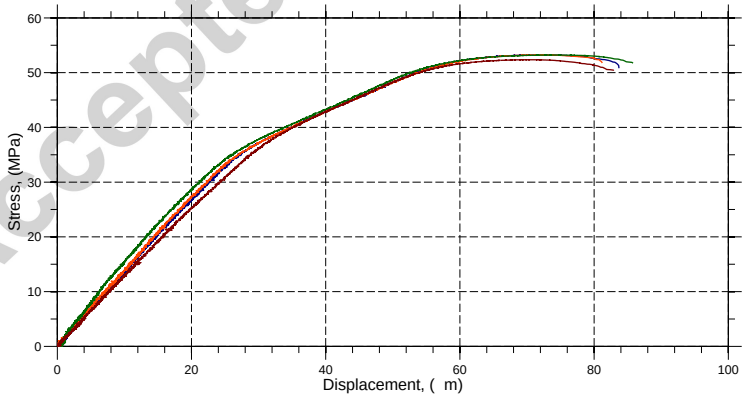

(c) Bond gap thickness = 2.5 mm

Figure 5: CDNT tests of the toughened adhesive, for a range of bond gap thicknesses with at least four repeats in each test.

1.57 and 1.36 for samples with bond gap thicknesses of 1.0 mm, 1.6 mm and 2.5 mm respectively. Also, it is important to note that the loading stress at which the kink occurs increases with a reduction in stress triaxiality.

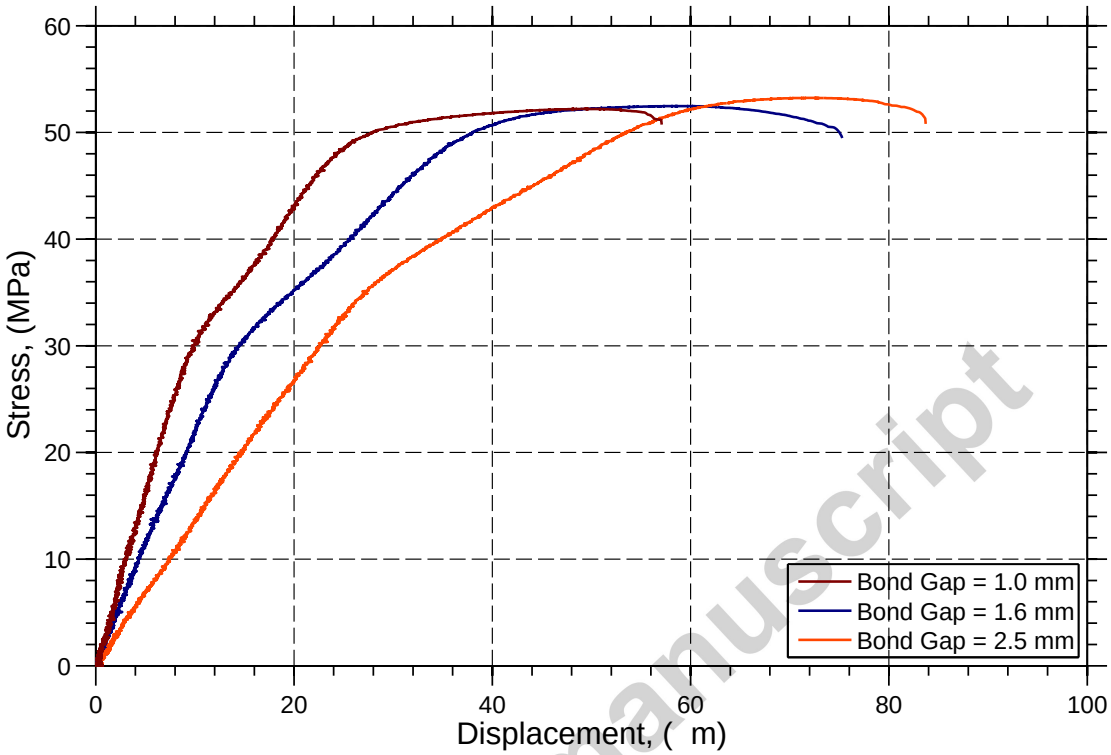

Figure 6: Comparison of the traction-displacement curves for tests that failed cohesively at each bond gap thickness.

For specimens with a bond gap thickness of 1.6 mm, a series of load-unload tests were completed to a maximum stress of 35 MPa, 45 MPa and 50 MPa, the results from which can be seen in Fig. 7. There are a number of observations from the unloading tests: (i) the unloading line is linear and does not contain a kink; (ii) the slope of the unloading line is less than that of the initial linear region but greater than the slope after the kink; and (iii) when the specimen is loaded further past the kink there is permanent deformation remaining when the load is removed.

4. Numerical Simulations

Numerical simulations of the CDNT tests were conducted using the Finite Volume method, which has been successfully applied to a variety of problems such as fluid-solid interaction, static and dynamic fracture of polymers and crack bifurcation [29, 7, 30, 31]. The method was implemented using the OpenFOAM software package, a C++ library for continuum mechanics. All substrates were considered to be linear elastic whilst the adhesive was treated as being non-linear elastic plastic defined by the uniaxial tension stress strain curve and conventional J2 plasticity. For the CDNT test an axisymmetric configuration was employed, containing between 90,000 and 100,000 cells. The geometry and boundary conditions are shown in Fig 8 and a typical mesh can be seen in Fig. 9.

4.1. Continuum Elasto-Plastic Simulations

Initial simulations of the CDNT test geometry were completed with the toughened adhesive specified as an non-linear elastic plastic continuum according to the experimental tensile stress strain curve. The

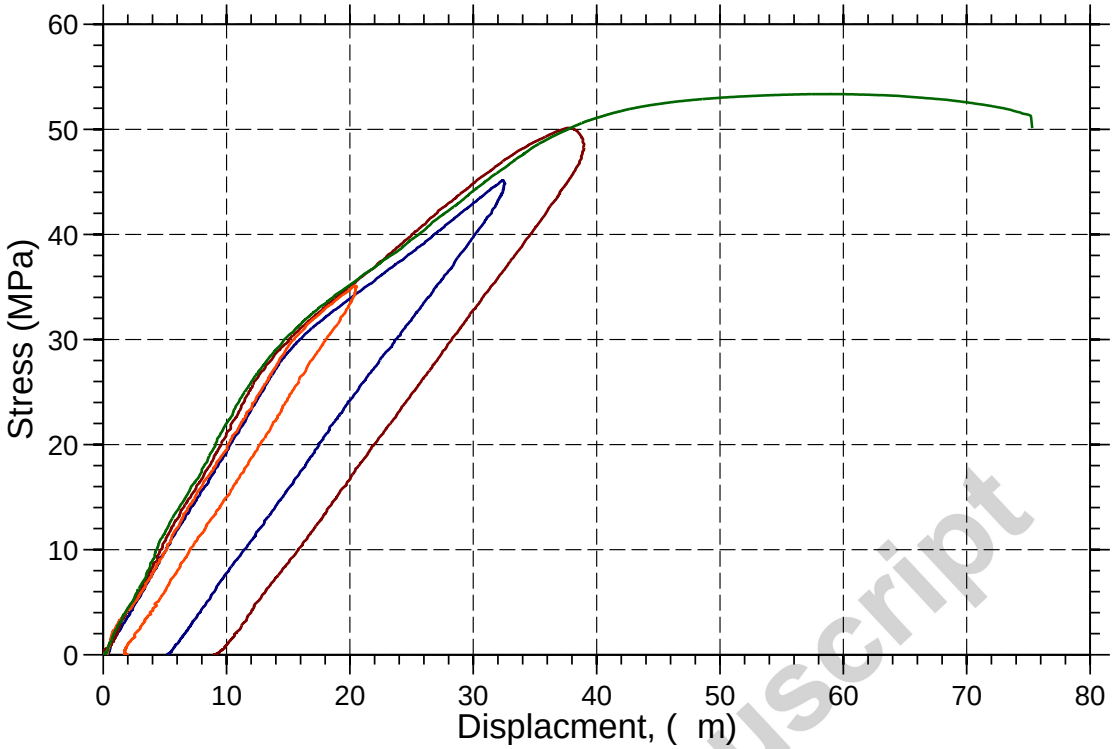

Figure 7: Results of a series of load-unload CDNT tests which were carried out to a maximum stress of 35 MPa, 45 MPa and 50 MPa, followed by unloading of the specimens. Here the bond gap thickness was 1.6 mm in each case.

displacement at the point corresponding to the position of the gauge marker was reported along with the average loading stress over the adhesive ligament. In Fig. 10 the results of this simulation are compared with the experimental data. The simulation accurately reproduces the initial stiffness of the experiment but is unable to capture the kink or any of the subsequent behaviour. The material model is pressure insensitive but it has been shown that yielding will still not occur around the kink point if pressure sensitivity is accounted for [23].

4.2. Fracture Simulations

For the remaining simulations fracture was incorporated using the Dugdale cohesive zone model (CZM). The CZM was applied at the boundary along the experimental crack path, as illustrated in Fig 8. For all simulations the cohesive strength was 52 MPa, based on the experimentally measured peak stress in the CDNT experiments. The intrinsic fracture energy, G_0, was selected as 2800 J/m^2 for every case as this gave reasonable agreement with the point of failure. All the cohesive faces are activated once the stress-displacement curve stops increasing. After this point the stress distribution remains constant within the specimen, simulations with the value for G_0 between 2000 J/m^2 and 4000 J/m^2 only affected the point of failure. The experimental and numerical results are shown in Fig. 11.

In the current *bonded* CDNT simulations the initial stiffness was accurately predicted and the numerical averaged peak stress σ_{peak} agreed closely with experiments and with the specified cohesive strength, i.e. $\sigma_{max} = \sigma_{peak} = 52$ MPa. Therefore, it can be concluded that there isn't a significant stress concentration effect and the experimentally measured peak stress represents the intrinsic cohesive strength of the material.

4.3. Stress Distributions

The stress distributions across the adhesive ligament were estimated from the computational points that lie on the midplane of the notch. Average stresses, representative of the conditions across the notch ligament,

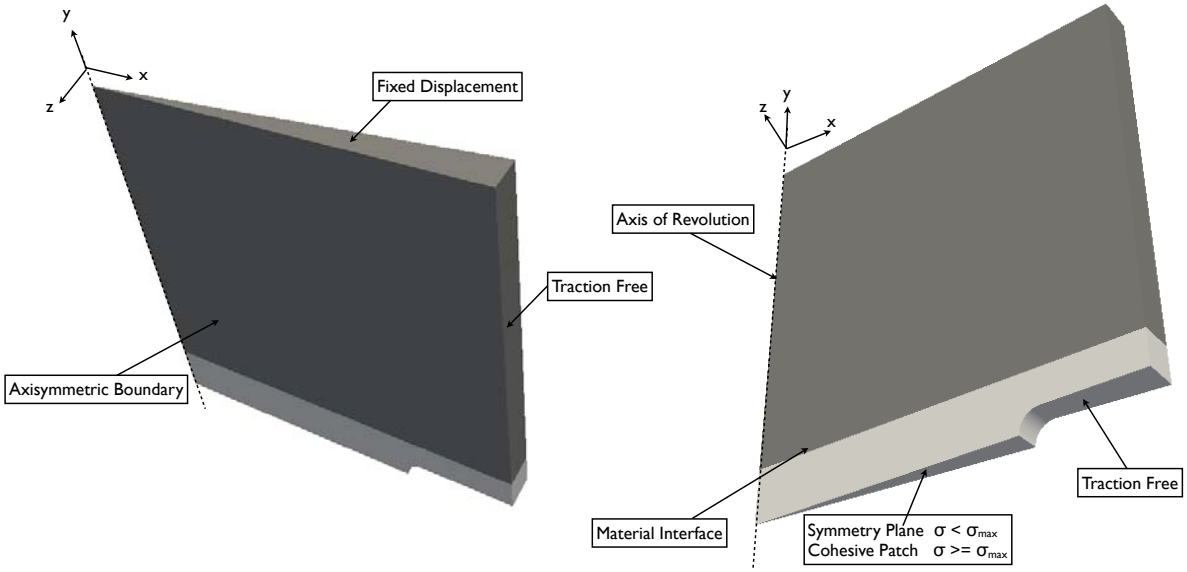

Figure 8: Boundary conditions in the CDNT simulations.

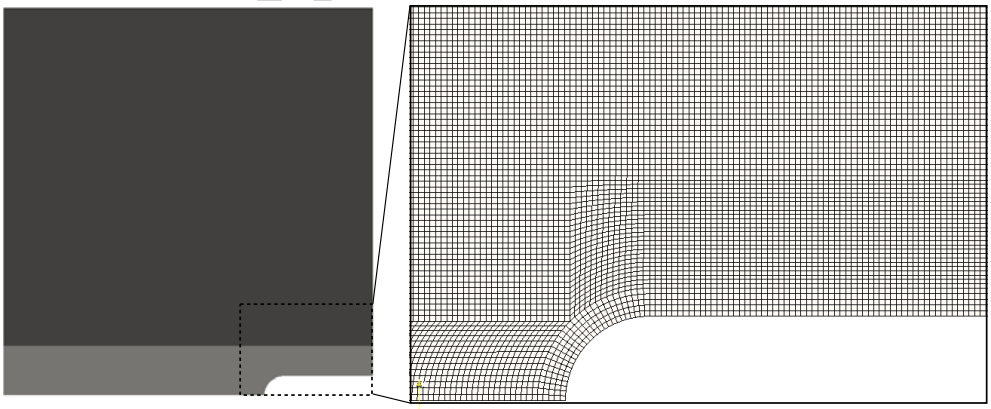

Figure 9: Typical mesh used in CDNT simulations.

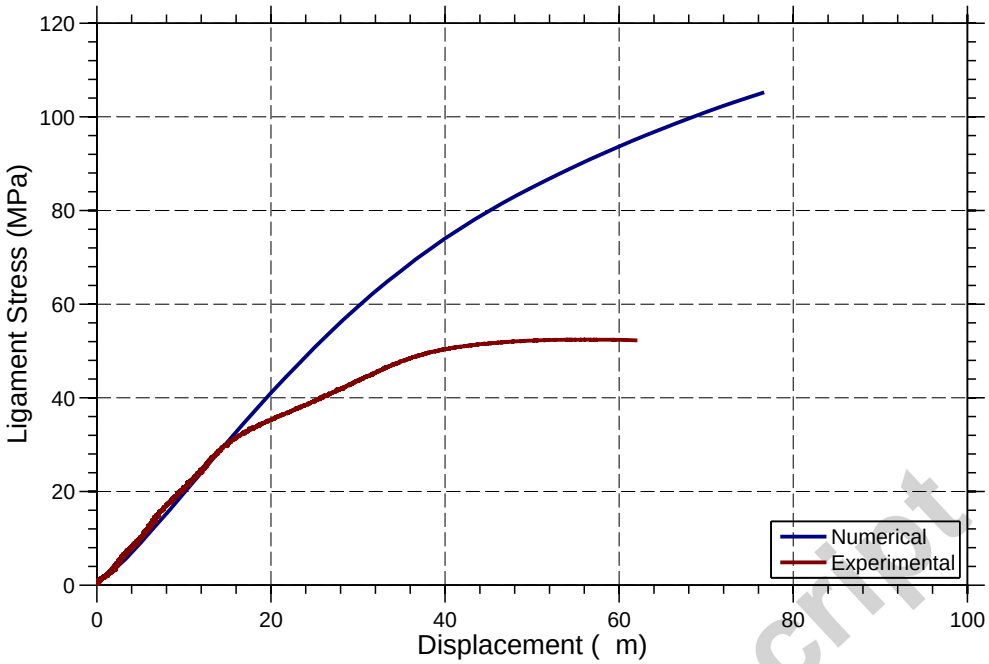

Figure 10: Comparison between elasto-plastic numerical simulation without active CZM and experimental results. The model is unable to capture the kink or subsequent deformation.

were calculated from the same distributions according to the following equation

$$\phi_{avg} = \frac{1}{A}\int_A \phi \, \mathrm{d}A \tag{4}$$

where ϕ is the quantity to be averaged, A is the area of the ligament and $\mathrm{d}A$ is the area of the cell face that lies on the mid-plane. For each bond gap thickness the variation of stress and constraint over the radius of the ligament are displayed in Figs. 12 and 13. The stress distributions are taken before the initiation of damage and are normalised against their respective average loading stress given by Eq.(4).

The change in constraint over the radius is shown in Fig. 12a. For all tests H is greatest at the centre and decreases monotonically with an increase in radius. H_{avg} is higher for specimens with lower bond gap thicknesses and increases from 1.37 to 2.09. This is a significantly higher constraint compared with the level of constraint in a bulk CDNT test where H varied between 1.0 and 1.4 [32].

The stress, σ_{yy}, is also plotted in Fig. 12b. The stress remains constant until relatively close to the edge of the specimen, where the presence of the notch begins to influence the stress state. The magnitude of stress concentration is greatest for the 2.5 mm specimen, where $\sigma_{yy}/\sigma_{yy}^{avg}$ is just greater than 2 at the tip of the notch.

Fig. 13a contains a graph of the hydrostatic stress distribution. The hydrostatic stress, σ_{hyd}, is relatively constant across the total radius and deviates the least from the average compared with the other stress distributions.

The von Mises stress distribution is included in Fig. 13b. The average normalised von Mises stress increases with bond gap thickness, or, increases with a decrease in constraint. The averaged stress distributions at the loading stress when the kink occurs are listed in Table 3 for each bond gap thickness. The average von Mises stress, σ_{vm}^{avg} is well below $\sigma_y^{0.2}$ in all tests, therefore significant yielding does not occur. This is also the case with pressure sensitive yielding [23]. This analysis conclusively rejects the hypothesis that the kink is due to a diffuse yielding mechanism.

Closer analysis of the average stress distributions in Table 3 reveals that σ_{hyd} is relatively constant across

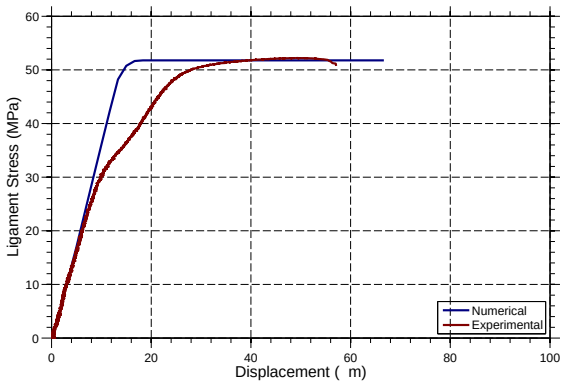

(a) Bond gap thickness = 1.0 mm

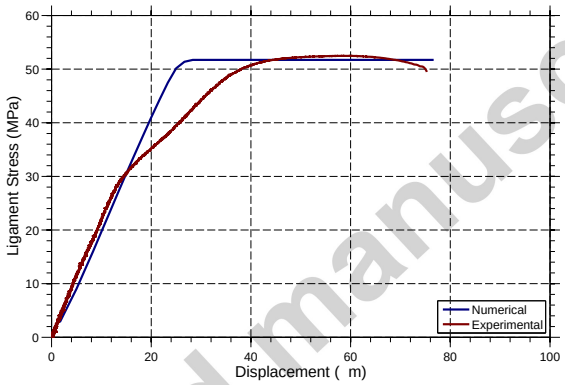

(b) Bond gap thickness = 1.6 mm

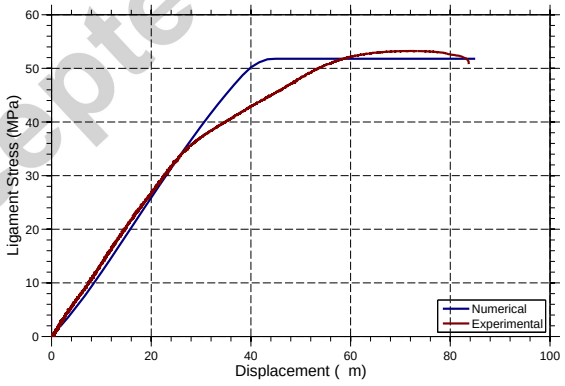

(c) Bond gap thickness = 2.5 mm

Figure 11: Comparison between numerical CDNT simulations and experiments for the range of bond gap thicknesses. G_0 has been arbitrarily chosen as 2800 J/m^2 in each case.

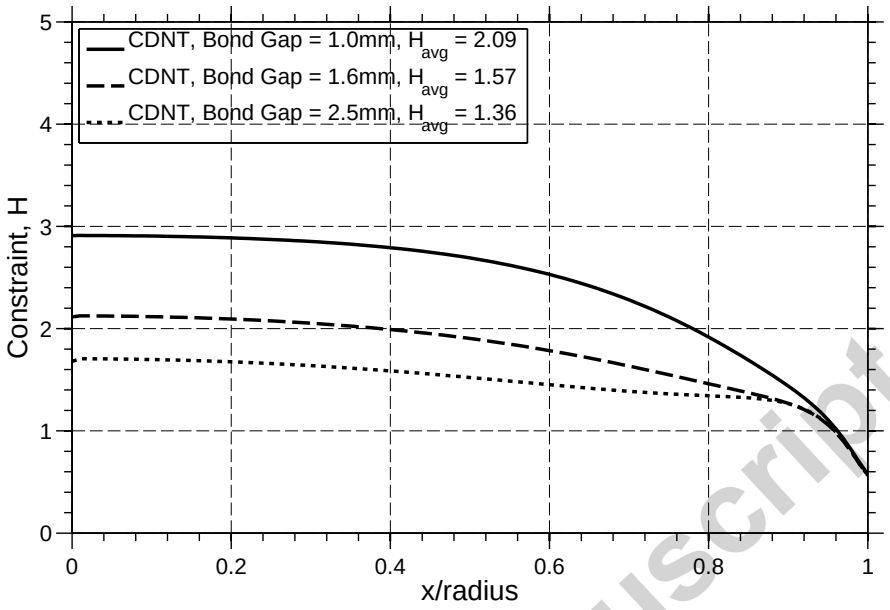

(a)

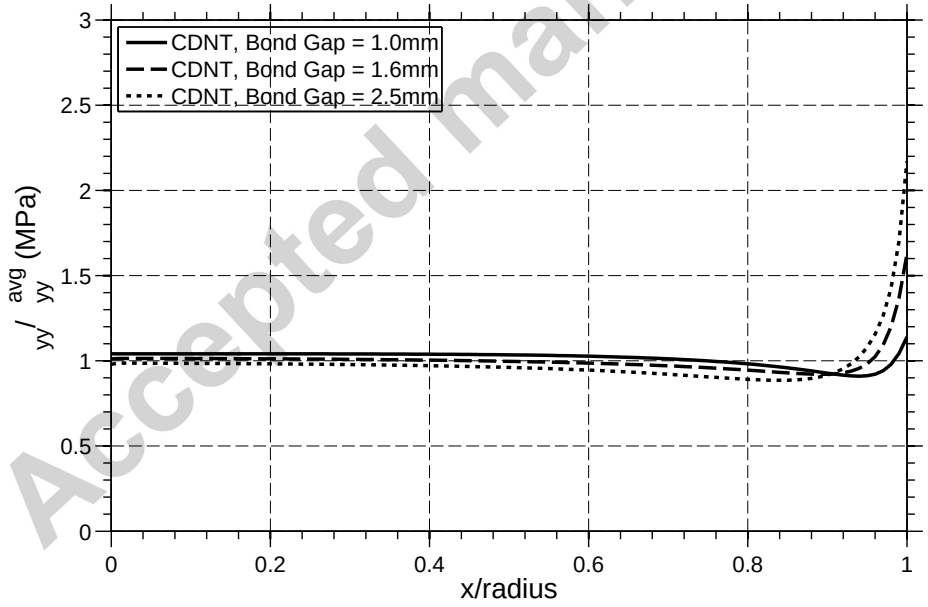

(b)

Figure 12: The distribution of (a) H and (b) σ_{yy} over the radius of the CDNT specimens prior to the initiation of damage for specimens with bond gap thicknesses of 1.0 mm, 1.6 mm and 2.5 mm.

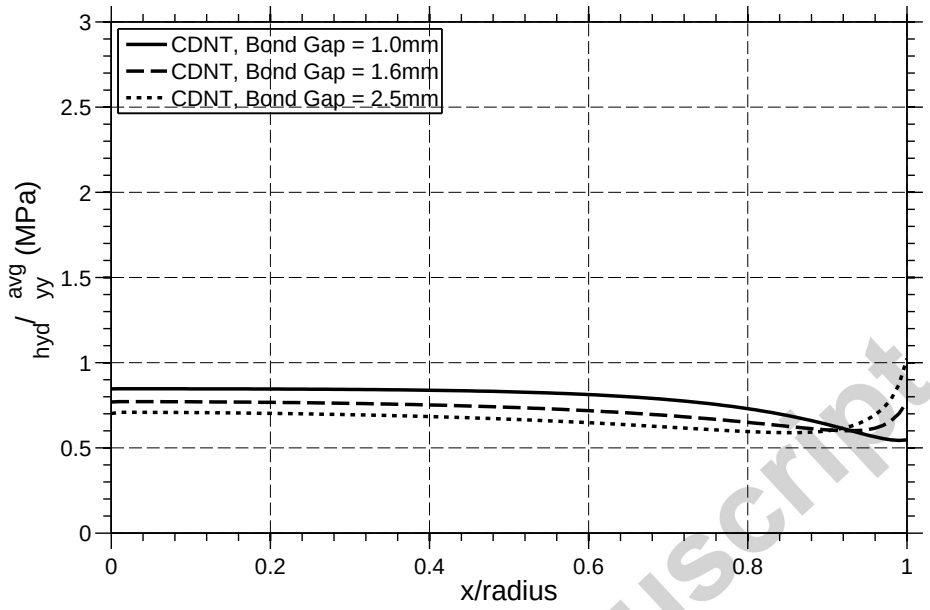

(a)

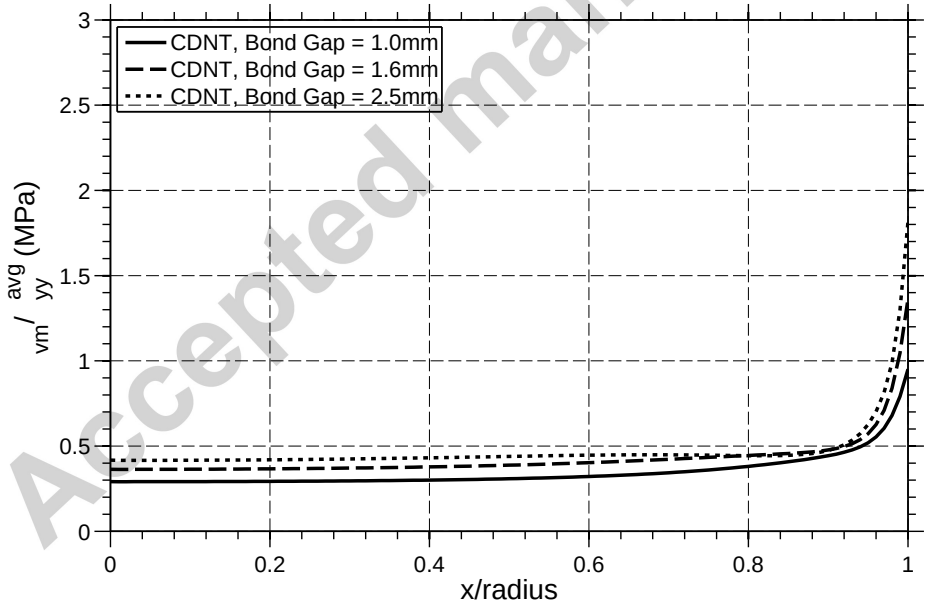

(b)

Figure 13: The distribution of (a) σ_{hyd} and (b) σ_{vm} over the radius of the CDNT specimens prior to the initiation of damage for specimens with bond gap thicknesses of 1.0 mm, 1.6 mm and 2.5 mm.

Table 3: Averaged parameters of the bonded CDNT tests at the kink in the experimental traction displacement curve. For the toughened adhesive $\sigma_y^{0.2} = 29$ MPa.

Bond Gap	σ_{yy}^{avg} (MPa)	H_{avg}	σ_{hyd}^{avg} (MPa)	σ_{vm}^{avg} (MPa)
1.0	30	2.09	22.3	11.7
1.6	32	1.57	22.0	15.1
2.5	35	1.36	23.0	18.2

the range of specimens at the instant the kink occurs. This is a significant finding and will be discussed later.

5. Analysis of Failure Mechanisms

Numerical simulations of the CDNT tests at each bond gap thickness revealed that the average level of constraint across the adhesive ligament lies within the stress triaxiality range typically encountered during adhesive joint fracture. Consequently, the failure mechanisms in the CDNT test are expected to be equivalent to the processes around the crack tip in an adhesive joint.

In this section, the possible mechanisms of material separation are proposed based on the traction displacement relationship measured in the bonded CDNT tests. As noted above, a characteristic feature of all CDNT tests was a sudden reduction in stiffness after initial linear loading, termed the "kink", as labelled in Fig. 14.

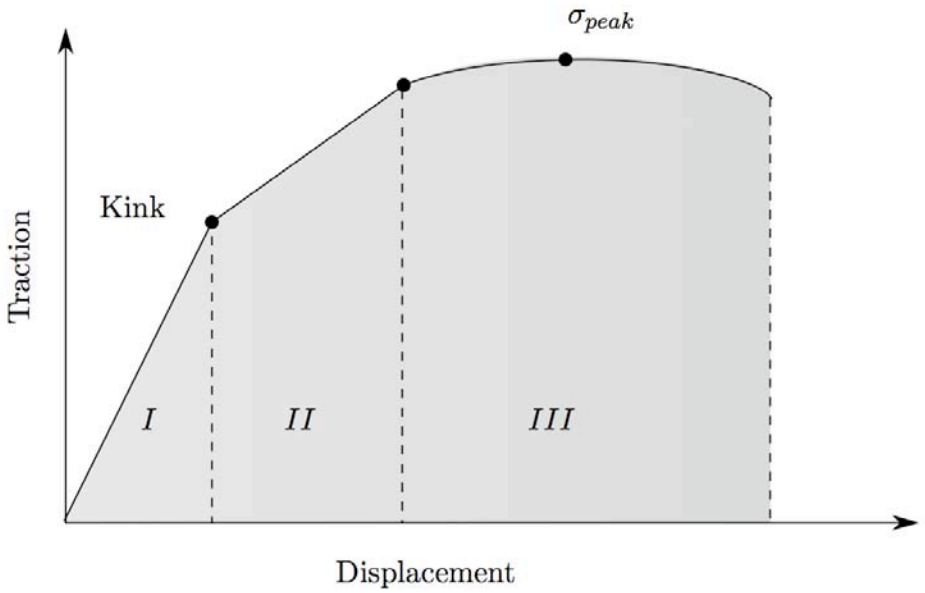

Figure 14: The three stages of the CDNT test and other points of interest.

5.1. The Interfacial Stress

Rubber particles have a low stiffness but a far greater bulk modulus [33]. Consequently, when located in a stressed polymer matrix the particles are in almost pure hydrostatic tension [34]. Numerical modelling

has also shown that the state of stress is uniform within the particle [15]. Therefore, under quasi-static conditions, the normal stress acting across the particle/matrix interface must equal the hydrostatic stress within the particle.

However, a stress concentration tensor, $\boldsymbol{B}$, [35] may be defined that relates the average *stress* in the composite material, $\bar{\boldsymbol{\sigma}}$, to the stress in the particle, $\boldsymbol{\sigma}^p$, i.e.

$$\boldsymbol{\sigma}^p = \boldsymbol{B} : \bar{\boldsymbol{\sigma}}. \tag{5}$$

The necessary equations to calculate $\boldsymbol{B}$, are given here but the method is described by Benveniste [35]. The fourth order elasticity tensor, $\boldsymbol{C}$ is:

$$C_{ijkl} = \lambda\delta_{ij}\delta_{kl} + \mu\left(\delta_{ik}\delta_{jl} + \delta_{il}\delta_{jk}\right) \tag{6}$$

where λ and μ are the Lamé constants given by $\lambda = K - 2/3G$ and $\mu = G$, where K is the bulk modulus and G is the shear modulus of the material. For spherical particles, the Eshelby equivalent inclusion tensor $\boldsymbol{E}$ is:

$$E_{ijkl} = \frac{5\nu - 1}{15(1-\nu)}\delta_{ij}\delta_{kl} + \frac{4 - 5\nu}{15(1-\nu)}\left(\delta_{ik}\delta_{jl} + \delta_{il}\delta_{jk}\right) \tag{7}$$

The Eshelby stress concentration tensor, $\boldsymbol{B}^{esh}$, is given by

$$\boldsymbol{B}^{esh} = \left[\boldsymbol{I} + \boldsymbol{C^m}\left(\boldsymbol{I} - \boldsymbol{E}\right).\left(\boldsymbol{S}^p - \boldsymbol{S}^m\right)\right] \tag{8}$$

where superscripts m and p refer to the matrix and particle respectively, $\boldsymbol{S}$ is the compliance tensor given by $\boldsymbol{S} = \boldsymbol{C}^{-1}$ and $\boldsymbol{I}$ is the fourth order identity tensor. This is only suitable for dilute mixtures where there is no interaction between particles. The Mori-Tanaka stress concentration tensor, $\boldsymbol{B}^{mt}$, is used for higher particle loading and is given by

$$\boldsymbol{B}^{mt} = \boldsymbol{B}^{esh}.\left[(1 - V_p)\boldsymbol{I} + V_p\boldsymbol{B}^{esh}\right]^{-1} \tag{9}$$

Numerical simulations of the CDNT tests revealed that the average hydrostatic stress, σ_{hyd}^{avg}, at the kink was $\simeq 22$ MPa. The corresponding average stress in the particles is then found using the expression below:

$$\boldsymbol{\sigma}^p = \boldsymbol{B}^{mt} : (\sigma_{hyd}^{avg} I) \tag{10}$$

where I is the second order identity tensor. To calculate the stress within a particle its material properties must be known accurately. The bulk modulus of rubber is typically taken to be $K = 2$ GPa [15]. Consistent elastic properties are $E_p = 2$ MPa and $\nu_p = 0.4998333$ which results in $\sigma_{hyd}^p/\sigma_{hyd}^{avg} = 19.26/22$. For this configuration, the results are very sensitive to a change in rubber material properties but are rather unaffected by the accuracy of V_p.

A primary conclusion of this analysis is that the particle/matrix interface stress is directly proportional to the macroscopic hydrostatic stress, under any typical triaxial mode of loading. Also, specifically for this adhesive, assuming that all the particles debond at the kink, and especially that the assumed particle properties are correct, then, the particle/matrix interface strength is around 19 MPa.

5.2. Porous Elasticity

After debonding, the particles no longer participate in the failure process and the applied load is re-distributed throughout the porous matrix. The Mori Tanaka model can also be used to predict the elastic properties of a porous solid as detailed by Zhao et al. [36]. For small spherical voids, the porous material is isotropic and its shear modulus, G, and bulk modulus, K, are related to the properties of the matrix, denoted by a subscript m, as follows:

$$\frac{K}{K_m} = 1 - \frac{1 - V_v}{1 - V_v\alpha_m} \tag{11a}$$

$$\frac{G}{G_m} = 1 - \frac{1 - V_v}{1 - V_v \beta_m} \tag{11b}$$

where V_v is the volume fraction of voids, equal to V_p if considering debonding; and α_m and β_m are given by:

$$\alpha_m = \frac{1}{3}\left(\frac{1+\nu_m}{1-\nu_m}\right) \quad \text{and} \quad \beta_m = \frac{2}{15}\left(\frac{4-5\nu_m}{1-\nu_m}\right) \tag{12}$$

Conventionally, the elastic properties of a material are given in terms of Young's modulus, E, and Poisson's ratio, ν, which are related to G and K with the expressions

$$E = \frac{9KG}{3K+G} \quad \text{and} \quad \nu = \frac{3K-2G}{2\,(3K+G)}. \tag{13}$$

By substituting Eqs.(12) into Eqs.(11) and entering the measured properties for the matrix, the porous elastic constants are found as $E_{por} = 1.35$ GPa and $\nu_{por} = 0.30$.

5.2.1. Comparison with Experiments

To produce a lower bound prediction for the elastic stiffness of the system with a porous matrix, numerical simulations of the bonded CDNT tests detailed in Section 4 were repeated, except with the adhesive layer properties altered to be linear elastic according to $E = 1.35$ GPa and $\nu = 0.30$. The results obtained with the porous elastic properties are shown in Fig. 15 along with the experimental results.

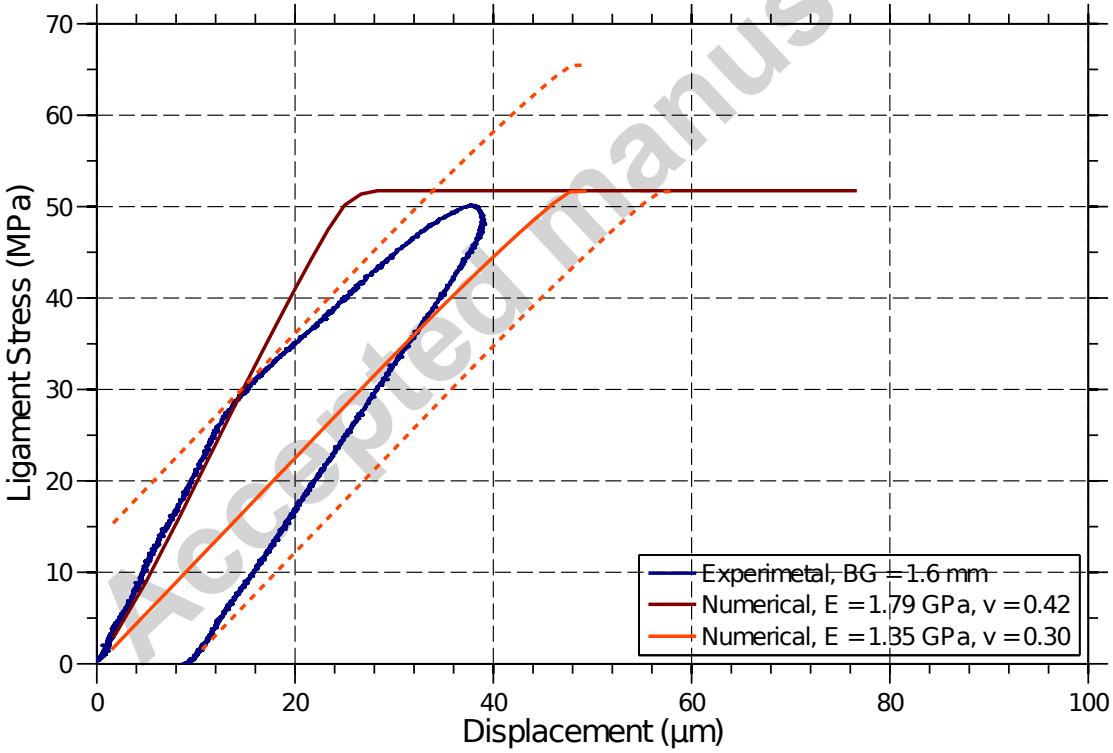

Figure 15: Comparison between experimental CDNT test and numerical predictions using: (i) toughened adhesive properties (solid red line) and (ii) predicted porous properties (solid orange line). The orange dashed lines are translations of the porous simulation for comparison with the stiffness in stage II during loading and unloading.

The stiffness of the system with porous elastic material properties is greater than experiments after the kink. As expected, the value of constraint reduces substantially in simulations with the porous material

properties compared to the non porous properties shown in Fig. 12. It is interesting to note however, that the value of H_{avg} for the three bond gap thicknesses is approximately 0.95.

5.3. Porous Yielding

Gurson [37] developed a continuum constitutive relation for the deformation of a porous material consisting of an elasto-plastic matrix. Central to the theory is a yield function, Φ, that predicts yielding according to the current volume fraction of voids, V_v; the current yield strength of the matrix, σ_y; and the current stress triaxiality, in terms of the macroscopic hydrostatic stress, σ_{hyd}, and the macroscopic von Mises stress σ_{vm}. Since then, the model has been analysed and developed by a series of authors.

Jeong and Pan [38, 39] modified the Gurson model to account for pressure sensitive yielding of the matrix. Their yield function is given as:

$$\begin{aligned}\Phi &= 0 = \left(\frac{\sigma_{vm}}{\sigma_y}\right)^2 + \left(1-\mu'_{vm}\frac{\sigma_{hyd}}{\sigma_y}\right)^2 \\ &\quad \times \left[2q_1V_v\cosh\left(q_2\frac{3+2\mu'_{vm}}{2\mu'_{vm}}\log\left(1-\mu'_{vm}\frac{\sigma_{hyd}}{\sigma_y}\right)\right) - 1 - q_3V_v^2\right] \end{aligned} \quad (14)$$

where $\mu'_{vm} = 0.485$ is the pressure sensitivity factor for the matrix [23]. Jeong performed FE simulations of a unit cell model over a broad range of stress triaxialities, void volume fractions and pressure sensitivity coefficients. In all cases, very close agreement between the unit cell model and Eq.(14) was obtained when $q_1 = 1.35$, $q_2 = 0.95$ and $q_3 = 1.35$.

The elastic stress distribution in the CDNT specimens after debonding, was approximated from numerical simulations with the derived porous material properties of $E = 1.35$ GPa and $\nu = 0.3$. Evaluation of the yield function in Eq.(14) along the cohesive patch at the loading stress when the kink occurs is shown in Fig. 16. In this case, under monotonic loading, the material is fully elastic if $\Phi < 0$ and plastic if $\Phi = 0$. For an elastic plastic material $\Phi > 0$ is not defined as the current stress distribution can never lie outside the yield surface. However, for an elastic analysis $\Phi > 0$ implies that the material has yielded and that the prohibited high stresses would be redistributed in the remaining material.

Clearly, from Fig. 16 yielding around the perimeter of the ligament is predicted immediately after debonding occurs. This yielding may account for the lower experimental stiffness in stage *II* than that predicted due to porous elasticity.

5.4. Final Separation

During the third stage of the CDNT tests the traction remains relatively constant reaching a peak stress, σ_{peak}, of around 52 MPa. Assuming that all particles have debonded the strength of the porous adhesive can be found from the cross sectional area of the matrix as:

$$\sigma^c_{UTS} = \sigma^m_{UTS}(1 - V_p) \quad (15)$$

where superscripts c and m refer to the composite and matrix, respectively. Using the measured matrix strength of 90 MPa, the predicted strength of the porous adhesive is 55.8 MPa. This is in reasonable agreement with the measured peak stress of 52 MPa, especially considering that the reduction in cross-sectional area due to void growth is not accounted for. It is also worth pointing out that, as expected, the rate of separation of the adhesive layer increases rapidly immediately prior to failure, as shown in Fig. 17. Images of the resulting fracture surface are shown in Fig. 18. It is clear that failure occurs without complete void coalescence, although significant void growth does occur. Measurement of the voids compared to the original particle size, has shown increases in diameter of up to 35%.

The failure characteristics of amorphous toughened polymers were discussed by Steenbrink et al. [40, 41], based on results obtained from their unit cell model. Steenbrink and co-workers found that for many polymers the shear band is stabilised after initial softening by hardening of the material, as was found in the compression data shown in Fig. 4 and the ligament draws with corresponding void growth leading to a diffuse distribution of plastic strain in the matrix.

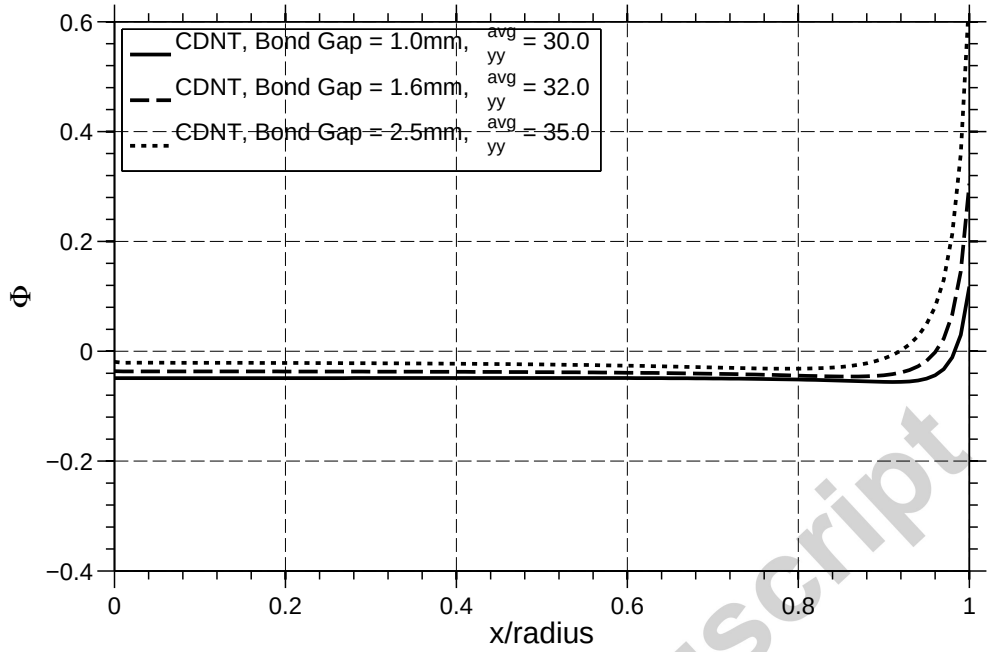

Figure 16: The Jeong yield function [38] evaluated across the adhesive ligament immediately after debonding, with $q_1 = 1.35$, $q_2 = 0.95$ and $q_3 = 1.35$.

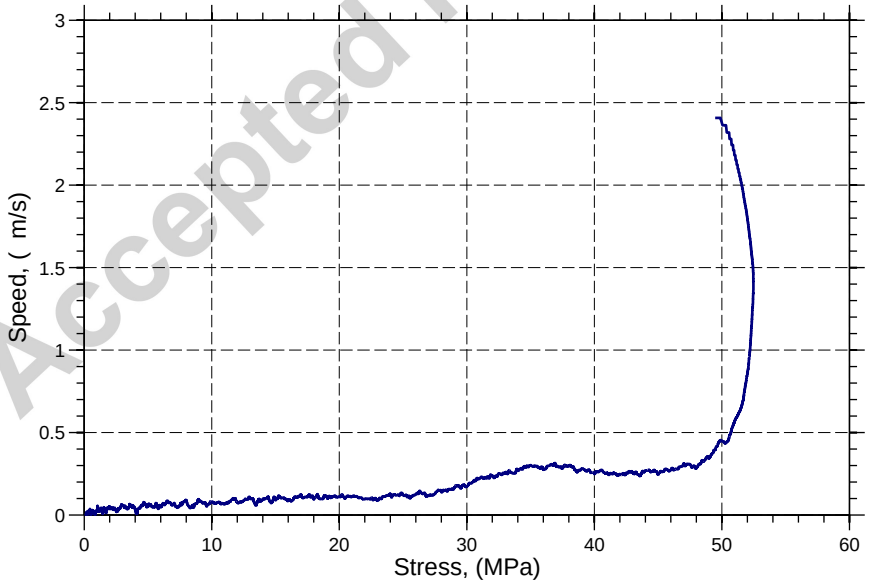

Figure 17: The relative speed of the gauge markings versus loading stress. As the stress reaches its peak the test accelerates rapidly.

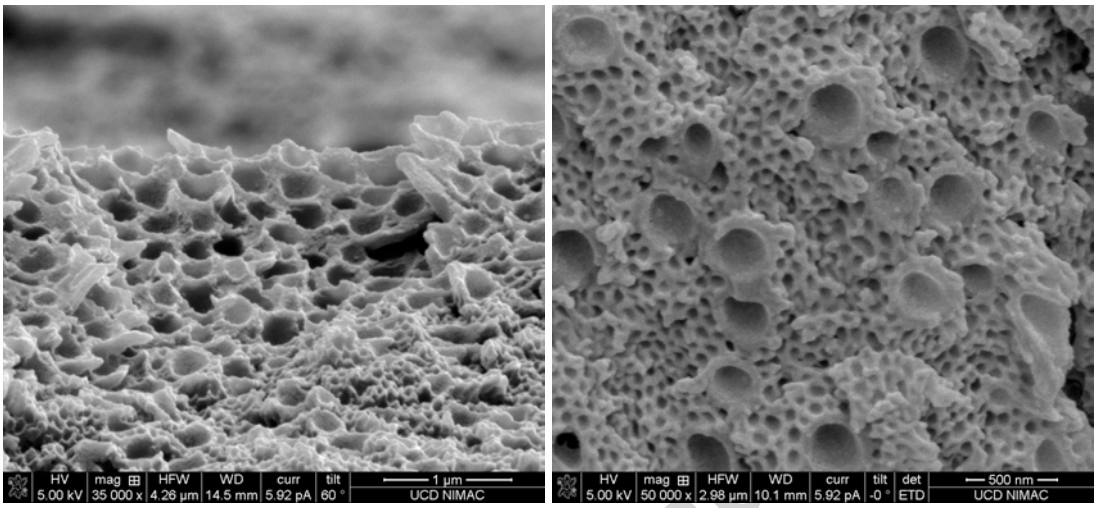

(a) (b)

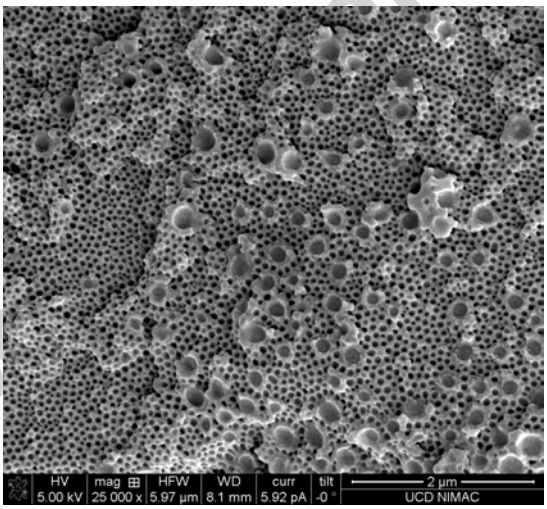

(c)

Figure 18: Fracture surfaces of the toughened adhesive with significant void growth.

6. Summary of Failure Evolution

6.1. Stage I

Stage I consists of elastic loading, concluding with an abrupt kink in the experimental traction-displacement curve. It is highly likely that the kink is due to the particle debonding/cavitation process, based on the breadth of evidence presented in the earlier sections.

The required yield stress for conventional or pressure dependent yielding was not reached in the bonded CDNT tests and so can be reliably dismissed as the source of the kink. Analysis of the stress distributions demonstrated that the kink occurs at a critical level of macroscopic hydrostatic stress. Further micromechanical analysis using the Mori-Tanaka model reveals that for rubber filled polymers the stress across the particle/matrix interface is directly proportional to the macroscopic hydrostatic stress. A critical interfacial stress for debonding is accepted as a criterion for particle debonding. Therefore it is concluded that the kink is due to particle debonding that occurs at a critical particle-matrix interface stress across all bond gaps.

It should also be noted that in uniaxial tension the macroscopic hydrostatic stress never exceeds 22 MPa, which accounts for the absence of a kink in the stress strain curve.

6.2. Stage II

Stage II begins after the kink and is structurally a porous solid since the particles have debonded in the ligament region of the CDNT and the load is redistributed throughout the matrix. It appears that plastic void growth initiates at this stage based on two porous material models. A lower bound estimate for the elastic stiffness of the system, based on porous matrix material properties, was still greater than the experimental stiffness during stage II. Therefore it seems porous yielding is the only mechanism that could account for the behaviour. Evaluation of a pressure dependent porous plasticity yield function indicates that yielding occurs once the particles have debonded in a narrow region around the edge of the sample, although it should be noted that the whole adhesive layer was considered porous for this analysis.

6.3. Stage III

In this work, the matrix initially softens but then the hardening rate increases. This encourages diffuse yielding over the process zone of the toughened adhesive resulting in a higher toughness than the bulk material. Final separation of the adhesive occurs by fracture of the ligament remaining between voids before complete coalescence can occur.

7. Conclusions

In this work a new experimental technique, the bonded CDNT test, was developed to measure the cohesive strength of a toughened adhesive at different levels of stress triaxiality. The stress triaxialities generated were between 1.36 and 2.09 and are comparable to the levels experienced near the crack tip in adhesive joints with metal substrates. It was found that the cohesive strength of the material was nearly constant and close to 52 MPa. This has not been observed by other authors where an increase in constraint, H, results in an increase in the measured peak stress [32, 20]. In those cases an increase in stress concentration at the root of the notch with constraint was reported which explains the experimental behaviour. The bonded CDNT test does not exhibit as strong a stress concentration with constraint, hence a constant failure stress is recorded. Furthermore, numerical modelling of the CDNT test with $\sigma_{max} = \sigma_{peak}$ reproduces the experimental peak stress. This demonstrates that separation occurs evenly across the ligament due to simultaneous loading of the cohesive faces. This is a significant finding, as it confirms that the measured peak stress is the intrinsic cohesive strength of the material.

The measured traction displacement curves also exhibited a distinctive kink, which is attributed to particle debonding at a critical hydrostatic stress. It was also found through the use of the Mori-Tanaka model that the macroscopic hydrostatic stress is proportional to the particle-matrix interface stress. This suggests that the method can be used as a measure of particle/matrix adhesion, but also that a critical macroscopic hydrostatic stress is a useful criterion for damage initiation in the adhesive layer.

[1] A. F. Yee, R. A. Pearson, Toughening mechanisms in elastomer-modified epoxies Part 1 Mechanical studies, Journal of Materials Science 21 (1986) 2462–2474.

[2] R. Pearson, A. Yee, Toughening mechanisms in elastomer-modified epoxies. ii: Microscopy studies, Journal of materials science 21 (1986) 2475–2488.

[3] R. Pearson, A. Yee, Influence of particle size and particle size distribution on toughening mechanisms in rubber-modified epoxies, Journal of materials science 26 (14) (1991) 3828–3844.

[4] T. Hsieh, A. Kinloch, K. Masania, A. Taylor, S. Sprenger, The mechanisms and mechanics of the toughening of epoxy polymers modified with silica nanoparticles, Polymer 51 (2010) 6284–6294.

[5] B. Johnsen, A. Kinloch, R. Mohammed, A. Taylor, S. Sprenger, Toughening mechanisms of nanoparticle-modified epoxy polymers, Polymer 48 (2007) 530–541.

[6] T. Pardoen, T. Ferracin, C. M. Landis, F. Delannay, Constraint effects in adhesive joint fracture, Journal of the Mechanics and Physics of Solids 53 (2005) 1951–1983.

[7] V. Cooper, A. Ivanković, A. Karač, D. McAuliffe, N. Murphy, Ž. Tuković, The effect of constraint on the fracture toughness of adhesively bonded joints, in: Proceedings of the 32nd annual meeting of the Adhesion Society, Savannah, 2009, pp. 33–35.

[8] T. Ferracin, C. Landis, F. Delannay, T. Pardoen, On the determination of the cohesive zone properties of an adhesive layer from the analysis of the wedge-peel test, International Journal of Solids and Structures 40 (2003) 2889–2904.

[9] V. Tvergaard, J. W. Hutchinson, The relation between crack growth resistance and fracture process parameters in elastic-plastic solids, Journal of the Mechanics and Physics of Solids (1992) 1377–1397.

[10] V. Cooper, A. Ivankovic, A. Karac, D. McAuliffe, N. Murphy, Effects of bond gap thickness on the fracture of nano-toughened epoxy adhesive joints, Polymer 53 (24) (2012) 5540–5553.

[11] P. Martiny, F. Lani, A. Kinloch, T. Pardoen, A maximum stress at a distance criterion for the prediction of crack propagation in adhesively-bonded joints, Engineering Fracture Mechanics 97 (2013) 105–135.

[12] K. Madhusudhana, R. Narasimhan, Experimental and numerical investigations of mixed mode crack growth resistance of a ductile adhesive joint, Engineering Fracture Mechanics 69 (2002) 865–883.

[13] B. Blackman, H. Hadavinia, A. Kinloch, J. Williams, The use of cohesive zone model to study the fracture of fibre composites and adhesively-bonded joints, International Journal of Fracture 119 (2003) 25–46.

[14] J. R. Rice, D. M. Tracey, On the ductile enlargement of voids in triaxial stress fields, Journal of the Mechanics and Physics of Solids 17 (1969) 201–217.

[15] X. Chen, Y. Mai, Micromechanics of rubber toughened polymers, Journal of materials science 33 (1998) 3529–3539.

[16] S. K. M. Ting, J. G. Williams, A. Ivankovic, Characterization of the Fracture Behavior of Polyethylene Using Measured Cohesive Curves. I: Effects of Constraint and Rate, Polymer Engineering and Science 46 (2006) 763–777.

[17] S. K. M. Ting, J. G. Williams, A. Ivankovic, Characterization of the Fracture Behavior of Polyethylene Using Measured Cohesive Curves. III. Structure–Property Relationships, Polymer Engineering and Science 46 (2006) 792–798.

[18] S. K. M. Ting, J. G. Williams, A. Ivankovic, Characterization of the Fracture Behavior of Polyethylene Using Measured Cohesive Curves. II. Variation of Cohesive Parameters With Rate and Constraint, Polymer Engineering and Science 46 (2006) 778 –791.

[19] T. Pardoen, I. Doghri, F. Delannay, Experimental and numerical comparison of void growth models and void coalescence criteria for the prediction of ductile fracture in copper bars, Acta Materialia 46 (1998) 541–552.

[20] K. Katnam, A. Comer, W. Stanley, M. Buggy, T. Young, Investigating tensile behaviour of toughened epoxy paste adhesives using circumferentially notched cylindrical bulk specimens, International Journal of Adhesion and Adhesives 37 (2012) 3–10.

[21] L. Asp, L. Berglund, P. Gudmundson, Effects of a composite-like stress state on the fracture of epoxies, Composites science and technology 53 (1) (1995) 27–37.

[22] D. Quan, A. Ivankovic, Effect of core-shell rubber (CSR) nano-particles on mechanical properties and fracture toughness of an epoxy polymer, Polymer 66 (2015) 16–28.

[23] D. McAuliffe, Fracture toughness characterisation of a nano-modified structural adhesive, Ph.D. thesis, University College Dublin (2012).

[24] P. Gabbott (Ed.), Principles and Applications of Thermal Analysis, Blackwell Publishing, Oxford, 2007.

[25] B. I. 15166-2:2000, Adhesive - methods of preparing bulk specimens - part2: Elevated-temperature-curing one-part systems, British Standards Institute (2000).

[26] E. Arruda, M. Boyce, Evolution of Plastic Anisotropy in Amorphous Polymers During Finite Straining, International Journal of Plasticity 9 (1993) 697–720.

[27] J. Williams, H. Ford, Stress Strain relationships for some unreinforced plastics, Journal of Mechanical Engineering Science 6 (1964) 405–417.

[28] T. Mori, K. Tanaka, Average stress in matrix and average elastic energy of materials with misfitting inclusions, Acta metallurgica 21 (5) (1973) 571–574.

[29] A. Karac, B. Blackman, V. Cooper, A. Kinloch, S. Rodriguez Sanchez, W. Teo, A. Ivankovic, Modelling the fracture behaviour of adhesively-bonded joints as a function of test rate, Engineering Fracture Mechanics 78 (6) (2011) 973–989.

[30] D. McAuliffe, A. Karać, N. Murphy, A. Ivanković, Transferability of adhesive fracture toughness measurements between peel and tdcb test methods for a nano-toughened epoxy, in: Proceedings of the 34th annual meeting of the Adhesion Society, Savannah (USA), 2011.

[31] N. Murphy, A. Ivankovic, The prediction of dynamic fracture evolution in PMMA using a cohesive zone model, Engineering fracture mechanics 72 (2005) 861–875.

[32] V. Cooper, The fracture behaviour of nano-toughened structural adhesive, Ph.D. thesis, University College Dublin (2010).

[33] D. Tabor, The bulk modulus of rubber, Polymer 35 (13) (1994) 2759–2763.
[34] C. Fond, Cavitation criterion for rubber materials: A review of void-growth models, Journal of Polymer Science Part B: Polymer Physics 39 (17) (2001) 2081–2096.
[35] Y. Benveniste, A new approach to the application of mori-tanaka's theory in composite materials, Mechanics of materials 6 (2) (1987) 147–157.
[36] Y. Zhao, G. Tandon, G. Weng, Elastic moduli for a class of porous materials, Acta Mechanica 76 (1) (1989) 105–131.
[37] A. Gurson, et al., Continuum theory of ductile rupture by void nucleation and growth: Part i-yield criteria and flow rules for porous ductile media, Journal of Engineering Materials and Technology 99 (1) (1977) 2–15.
[38] H. Jeong, A new yield function and a hydrostatic stress-controlled void nucleation model for porous solids with pressure-sensitive matrices, International journal of solids and structures 39 (5) (2002) 1385–1403.
[39] H. Jeong, J. Pan, A macroscopic constitutive law for porous solids with pressure-sensitive matrices and its implications to plastic flow localization, International journal of solids and structures 32 (24) (1995) 3669–3691.
[40] A. Steenbrink, E. Van der Giessen, P. Wu, Void growth in glassy polymers, Journal of the Mechanics and Physics of Solids 45 (3) (1997) 405–437.
[41] A. Steenbrink, E. Van Der Giessen, P. Wu, Studies on the growth of voids in amorphous glassy polymers, Journal of materials science 33 (12) (1998) 3163–3175.